Monitoring corrosion-induced concrete cracking adjacent to the steel-concrete interface

(article starts on next page)

ORIGINAL ARTICLE

Monitoring corrosion-induced concrete cracking adjacent to the steel-concrete interface

Andreas Alhede (ID) · **Jelke Dijkstra** · **Karin Lundgren**

Abstract Substantial research effort has been devoted on linking corrosion-induced cracking of concrete with the internal corrosion damage level. Still, numerical models of the corrosion and cracking process require internal parameters, that cannot be directly evaluated from experimental data. Therefore, this study provides a novel experimental method for monitoring the effects of steel corrosion adjacent to the steel-concrete interface. This non-destructive method is suited for small-scale laboratory-made specimen, and was designed to provide missing information required for subsequent calibration of numerical models. Hollow steel bars were cast into concrete and subjected to accelerated corrosion using the impressed current technique. The deformations of the hollow steel bars were measured using distributed strain sensing in an optical fibre, attached to the inner surface of the hollow steel bars. After the corrosion period, X-ray Computed Tomography scans were performed to evaluate concrete cracking and corrosion level. The results reveal a non-uniform distribution of strain around the perimeter of the steel, indicating a non-uniform radial stress distribution. The non-uniformity correlated very well with the position of the corrosion-induced cracks; with extension hoop strains in the steel at the location of these cracks and contraction hoop strains in between. Further, the corrosion level varied around the perimeter, with higher values near cracks. The combination of non-destructive monitoring techniques used in this study on small-scale laboratory-made specimens show great potential to reveal new insights on how the corrosion pattern, corrosion-induced cracking of the concrete cover and stress (indirectly measured through the strain in the steel) interact throughout the corrosion process.

Jelke Dijkstra and Karin Lundgren have contributed equally to this work.

A. Alhede (✉) · K. Lundgren
Division of Structural Engineering, Chalmers University of Technology, 41296 Gothenburg, Sweden
e-mail: andreas.alhede@chalmers.se

J. Dijkstra
Division of Geology and Geotechnics, Chalmers University of Technology, 41296 Gothenburg, Sweden

1 Introduction

Corrosion of steel is the most common deterioration mechanism in reinforced concrete (RC) structures [1]. Climate change is expected to result in the intensification of environmental loads, which will exacerbate

this issue [2–5]. When corrosion products are formed at the steel-concrete interface (SCI), a volume increase takes place, eventually cracking the concrete cover. Furthermore, the reduction of steel cross-sectional area is very challenging to quantify, yet it can result in a decreased stiffness and load-carrying capacity of the structure.

In natural environments, the initiation and propagation of steel corrosion in concrete occurs gradually over a long period of time. Therefore, a significant portion of the experimental research has been carried out under accelerated conditions, purposely designed to increase the corrosion rate.

The possibility of linking the steel cross-sectional area reduction to corrosion-induced crack width and pattern, which can easily be observed on the surface of the concrete structure during an inspection, is of major interest for engineering practice. Experimental investigations have, however, shown a wide scatter in corrosion damage related to crack width [6, 7]. There are several reasons for this scatter, including but not limited to concrete quality, geometry and variations in corrosion morphology. Another factor contributing to this variability is the high corrosion rate in accelerated corrosion tests, which has been demonstrated to impact both crack width and pattern [8]. This phenomenon can be partially attributed to the influence of the corrosion rate on the type of corrosion product that forms within the sample [9], leading to differences in the volumetric expansion coefficient of the corrosion products. Furthermore, in a study by [7], the influence of freezing and thawing in natural environments was discussed as a possible reason for the discrepancies between experimental research from accelerated environments and research conducted on natural corroded specimens.

With improved knowledge of the corrosion and cracking processes, there is a potential to model the underlying physical processes more accurately and explain at least parts of this scatter. In attempts to do so, major research efforts have been invested into modelling of the corrosion-induced cracking process, for example [10–13]. Ožbolt et al. [14] showed in analyses that the expansion process is non-homogeneous, leading to non-uniform radial stress at the surface of the steel. To verify and calibrate the model, they highlighted the need for experimental work.

It is important to note, that the development of the corrosion and cracking processes is non-linear with respect to time. This evolution of damage should be considered in studies of corrosion-induced cracking. Non-destructive monitoring techniques are required to properly investigate the corrosion and cracking processes in individual test specimens. However, only a limited number of non-destructive techniques for monitoring changes at the SCI have been employed [15], despite numerous studies on the local properties of the SCI [16] and investigations into factors that affect steel corrosion [17].

This paper explores a new approach for non-destructive monitoring of corrosion-induced deformations adjacent to SCI in laboratory specimens, in an attempt to bridge the gap between numerical and experimental research on corrosion-induced cracking in RC. The main aim was to design a novel test setup such that the interaction between corrosion-induced strains in the steel, concrete cracking and corrosion level could be studied in well-controlled small-scale laboratory-made specimens. Cylindrical RC specimens of different configurations were cast and subjected to accelerated corrosion, using the impressed current technique [18]. The configurations were selected to investigate the influence of different depths of the concrete cover as well as prior exposure to freezing and thawing cycles. The corrosion and cracking processes were studied adjacent to the SCI using distributed strain sensing in optical fibres that were glued inside hollow steel reinforcement bars. Strain measurements from the fibres were continuously monitored throughout the accelerated corrosion process. Following this phase, X-ray Computed Tomography (XCT) was employed to acquire image data of the specimens, enabling the study of concrete cracking and corrosion level.

2 Experiments

The experimental setup was designed to study the interaction between corrosion-induced deformations, measured from the inside of reinforced concrete samples, corrosion level and concrete cracking using a distributed optical fibre system and X-ray Computed Tomography (XCT). Open-ended, plain, steel tubes (hollow reinforcement bars) were cast in concrete and subjected to accelerated corrosion, while continuously monitoring the strain at the inner surface of the hollow steel bars with distributed optical fibres. After the

corrosion period, most of the specimens were scanned using XCT, from which cracking and corrosion level were evaluated. A timeline of the test procedure is shown in Fig. 1. In the following, the experimental programme, material and methods are elaborated.

2.1 Experimental programme

The experimental programme consisted of four different test conditions as listed in Table 1. In addition to the reference tests without accelerated corrosion, the impact of concrete cover thickness and prior freezing damage on the steel corrosion was investigated in additional test types. In total, eleven specimens were included in the experimental programme. The dimensions of the specimens were chosen to ensure a concrete cover thickness of reasonable size compared to the ones used in real structures, while simultaneously achieving a sufficiently high resolution in the XCT scans. Further, the wall thickness and the inner radius of the hollow steel bar were chosen to ensure that the strain on the inside was measurable [19]. All specimens were 100 mm long. The cross-sectional diameter varied from 88 mm for series C30, FC30 and R30, to 128 mm for series C50. A hollow steel bar with outer diameter 28 mm and a wall thickness of 2 mm was cast in the centre of each specimen. The steel bar protruded 10 mm from the bottom surface, see Fig. 2.

The hollow steel bars were manufactured from a 32 mm reinforcement bar, type K500C-T, using a lathe. The ribs were removed by milling the bar and the hollow section was obtained by drilling. The weight of each steel bar prior to and after the experiment was documented with a precision balance that had an accuracy of 0.01 g. The outer surface of the hollow steel bars was scanned using a portable 3D scanner before casting took place, and for two specimens of type C50, the steel bars were cleaned and scanned again after the corrosion experiment. The 3D scanner had a spatial resolution of 50 μm. Cleaning was done through sandblasting to remove fragments of cement paste and corrosion products. A previous study has demonstrated that sandblasting is a reliable cleaning method [20].

In Table 2, the concrete mix proportions and mechanical properties are given. The concrete was cast with cement type CEM II/A-LL 42.5R [21] and a water to cement ratio of 0.43. The concrete cured for 39 days before the material strength was evaluated from tests on cylindrical specimens (diameter 100 mm and length 200 mm). The compressive and tensile splitting strength were measured in accordance with [22] and [23], respectively.

2.2 Freezing and accelerated corrosion

Prior to accelerated corrosion, the specimens of type FC30 were subjected to freezing and thawing cycles. The specimens were immersed in water for a short time and thereafter wrapped in plastic film to prevent drying and subsequently placed in a climate chamber. The samples were subjected to five temperature cycles between a maximum and minimum temperature of 20 °C and −16 °C, as shown in Fig. 3. The period of each cycle was 14 h.

The accelerated corrosion was carried out in a climate room where the ambient room temperature
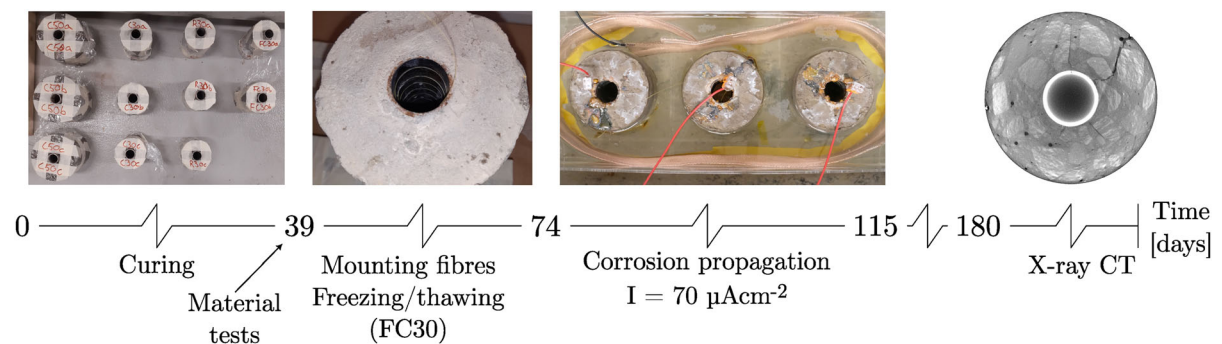

Fig. 1 Timeline of the experiments. Material tests took place 39 days after casting. The corrosion propagation period started 74 days after casting and lasted for 41 days. Specimens of types C30, FC30 and R30 were scanned using XCT approximately 180 days after casting

Table 1 Experimental programme: Specimen type, number of specimens, id, and type of experiment

Type	Number of specimens	Specimens ID	Type of experiment
C30	3	C30a-c	Corrosion
C50	3	C50a-c	Corrosion
FC30	2	FC30a-b	Frost and corrosion
R30	3	R30a-c	Reference
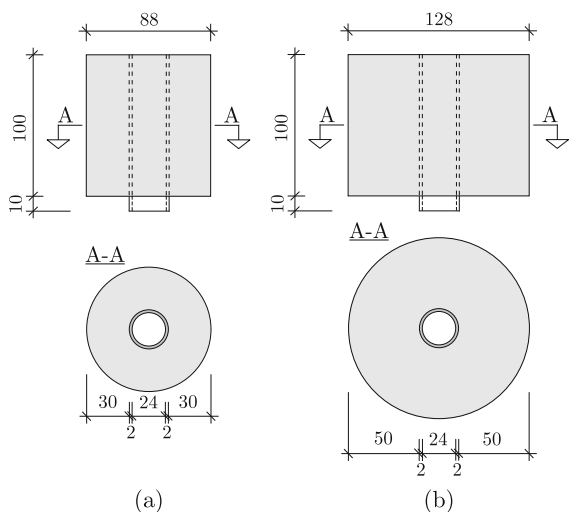
Fig. 2 Geometry of specimens in series **a** C30, FC30, R30 and **b** C50

Table 2 Concrete mix proportions and mechanical properties measured 28 days after curing

| Concrete mix proportions	
Water (kg m^{-3})	211.0
Cement (kg m^{-3})	490.0
Crushed aggregates (4/16 mm) (kg m^{-3})	948.0
Sand (0/4 mm) (kg m^{-3})	656.0
Sodium chloride (kg m^{-3})	4.9
Mechanical properties	
Compressive strength (MPa)	47.2
Tensile splitting strength (MPa)	4.08

and relative humidity was controlled and monitored continuously throughout the experiment. Prior to this phase, a visual inspection of the specimens was performed and no cracks could be observed with the naked eye. The specimens were placed in plastic containers with outlets for the protruding part of the steel in the bottom. Water leakage from the containers

was prevented by adding a layer of lubricant grease at the interface between the specimen and the bottom surface of the container, as shown in Fig. 4. A saline water solution (3 % NaCl) was added to the water in the containers associated to C30, C50 and FC30, whereas tap water was used for R30.
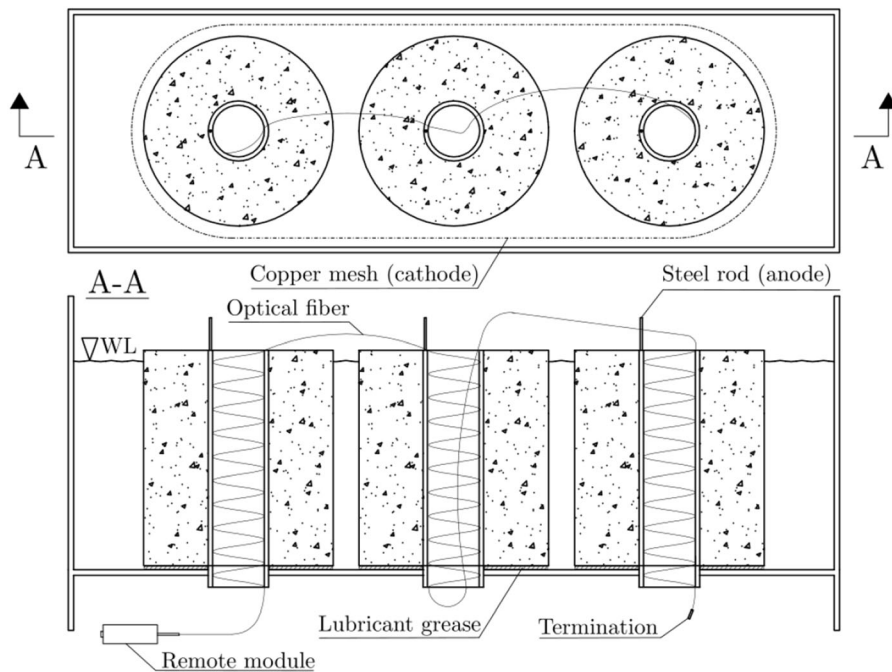
To accelerate corrosion, electrical current was applied to steel rods, welded to the hollow steel bars, and a copper mesh, acting as a cathode, was placed around the specimens to close the electrical circuit. The applied current density was limited to $70 \mu A$ cm^{-2}, which is considered to be a reasonable value to balance the conflicting requirements of mimicking natural corrosion and the need for short duration corrosion tests [24]. A custom made constant current source with multiple channels was used to apply an electrical current for a period of 41 days. This current source maintained the current density by adjusting the magnitude of the potential difference when the electrical resistivity in the sample changed.

2.3 Optical fibre sensors

An optical distributed sensor interrogator [25] was used to measure the distributed strains along an optical fibre. Polyimide coated optical fibres [26] with a sensor diameter of 155 μm, were glued in a helical shape to the inner surface of the hollow steel bar. A special plastic tool was designed to secure the fibre in place during the mounting process, see Fig. 5a. At mounting, a fibre was wound around the tool and secured with tape. Thereafter, the tool with the fibre attached was placed inside the hollow steel bar and the tape was removed. The helix of the fibre was achieved by twisting the tool along its longitudinal axis. When the helical shape was obtained, the fibre was bonded to the steel along three lines (illustrated by the solid black arrows in Fig. 5b), in the longitudinal direction of the bar using a polypropylene glue. The tool was there-after carefully removed and the remaining part of the fibre was glued to the steel. The gluing process was
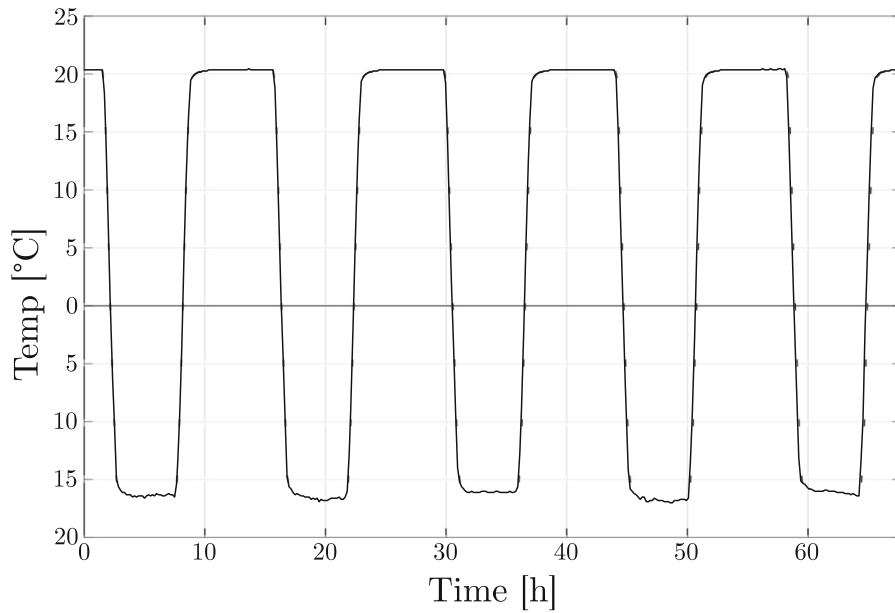
Fig. 3 Ambient air temperature during the freezing and thawing cycles applied to FC30

Fig. 4 Experimental setup for test types C30, C50 and FC30. Electrical current was applied to steel rods, welded to the steel bars, and a copper mesh, acting as a cathode, was placed around the specimens to complete the circuit

challenging, hence the exact spacing between turns varied slightly. The intended spacing between each turn was 10 mm, and for most specimens, 10 turns were made within one specimen. However, some specimens had fewer turns (but still nominal spacing 10 mm). E.g. for specimen C30a, approximately six turns were successfully mounted inside the hollow steel bar. Due to limitations in number of channels

Fig. 5 Process of gluing the fibre on the internal surface of the hollow steel bar. **a** An optical fibre wound around the arms of the tool, restrained with tape. **b** Positioning of the fibre inside the hollow steel bar. The fibre obtained its helical shape by removing the tape and by rotating the tool around its length, as indicated by the dashed arrow. The fibre was bonded to the steel by gluing the parts in between the plastic arms (solid black arrows). **c** Removal of the tool and additional gluing

available in the measurement system, one continuous fibre was attached to all specimens of each type.

The fibre sensors were re-keyed prior to the corrosion experiment, i.e. a new reference configuration was initialised for each fibre. Hence, all strain measurements are relative to the strain at the start of the accelerated corrosion phase. The gauge length of the sensors in the optical fibre and the measurement rate per channel were configured to 2.6 mm and 6.25 Hz, respectfully. However, due to the presence of significant strain gradients between the gauges, the occurrence of missing entries (dropouts) increased over time. Hence, at day sixteen in the corrosion experiment, the configurations of the measurement system were adjusted. The length between gauges and measurement rate were adjusted to 0.65 mm and 2.08 Hz, which improved the quality of the recorded data. Although strains were continuously monitored by the instrument throughout the corrosion period, data was only recorded from with an interval of

20 min by opening and closing a network connection. Every time the connection was open, several readings of the streaming data were executed. For each reading, missing entries along the distributed fibre were replaced with a linear interpolation of neighbouring non-missing entries. Outliers in the data were treated in an analogous way. An outlier was defined as a value greater than three times the scaled median absolute deviation from the median of the data, with a scaling factor $k = 1.4826$, assuming a Gaussian distribution. Subsequently, the mean strain for each gauge was calculated.

The suitability of the instrumentation strategy was evaluated by testing the response of a single instrumented hollow steel bar in a pressure chamber. An optical fibre was attached to the inner surface of the hollow steel bar in a similar helical shape as the corrosion experiments. The outer surface of the hollow steel bar was subjected to a uniformly distributed hydraulic pressure of different magnitudes, whilst

strain measures were recorded in the fibre. A linear elastic 3D finite element analysis of the loaded steel bar was carried out to evaluate the strains in this geometry. The strain in the simulated optical fibre was evaluated from the finite element analyses by the use of embedded reinforcement [27] with low stiffness in the same shape as the fibres in the test, assuming a perfect bond. For the steel, a modulus of elasticity of 200 GPa was assumed whilst a stiffness close to zero was assumed for the optical fibre. The steel was discretised into 76 solid elements along the perimeter, 100 solid elements along the length and two solid elements in the radial direction of the steel. The response at different external gauge pressures is shown in Fig. 6 for the experiment and the FE analyses. Generally, a good agreement between measured strain values and the calculated values is obtained. The differences at the ends of the hollow steel bar are likely due to boundary effects at the connection between the bar and the pressure chamber. The latter are inconsequential for the application in mind. Further, there is a tendency for the measured strains to fluctuate around the analysis result in the mid region of the tube. This may be attributed to the gluing method, as the number of fluctuations agrees with the number of turns of the helix, or to small variations in the wall thickness of the tube. The size of this fluctuation was however small in

comparison to the measured response. For pressures of 5 MPa and 15 MPa, this difference is below 8.6% and 6.8%, respectively. Thus, the strain measurements are considered to be reliable.

2.4 X-ray computed tomography

After the corrosion phase, the specimens of types C30, FC30 and R30 were scanned in a RX EasyTom150 tomograph. The XCT scan utilised an X-ray source configured with a voltage of 150 kV and a current of 200 mA. The source was filtered with a 0.3 mm thick iron sheet and a 0.35 mm thick copper sheet, to reduce beam hardening. The source-detector distance was 668.36 mm whilst the source-object distance was 149.77 mm. In order to accommodate the large size of the specimen, whilst obtaining the highest attainable resolution, two radiographies were acquired on each rotation position, where the detector is shifted horizontally. Additionally, the tomography was stacked in the vertical direction in four sequences, with 2880 radiographies taken over 360 ° of each stack. The acquisition rate of the flat panel detector was six frames per second and for each radiography, three frames were averaged. In total, this acquisition rate resulted in 11520 radiographies for each horizontal detector position, hence 23040 radiographies were
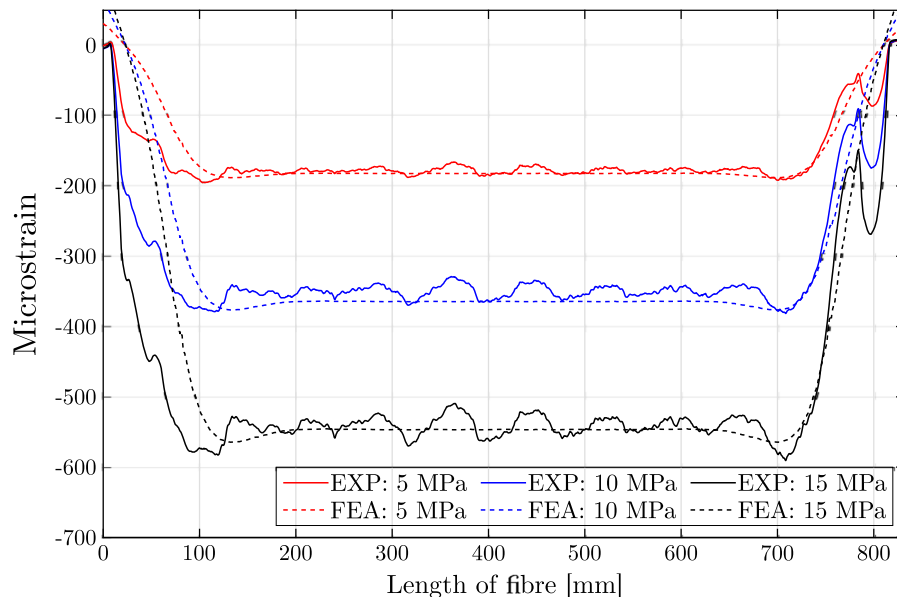
Fig. 6 Measurements of the strain in the fibre when a single instrumented hollow steel bar was subjected to a uniformly distributed hydraulic pressure on the outer surface of the steel in a pressure chamber. Experimental and numerical results, respectively

stitched together for a single scan. Subsequently, the tomographies were reconstructed using Filtered Back Projection, resulting in a final cubic voxel size of 28.46 μm. The tomography data was used to measure the corrosion level and for qualitative studies of concrete cracking.

2.5 Corrosion level

The corrosion level was evaluated from measurements of the steel cross-sectional area before and after corrosion. The corrosion level was computed as

$$C_l = 1 - \frac{A_{\mathrm{cor}}}{A_{\mathrm{uncor}}} = 1 - \frac{(r_{\mathrm{cor}} - r_i)^2}{(r_{\mathrm{uncor}} - r_i)^2}, \qquad (1)$$

where A_{uncor} and A_{cor} are the steel cross-sectional area before and after corrosion, respectively; r_{uncor} and r_{cor} are the radius before and after corrosion, respectively, and r_i is the inner radius of the hollow steel bar. Note that the inner radius of the steel bar is assumed not to be affected by corrosion, as was also visually observed after the corrosion period. The non-corroded cross-sectional area and radius were evaluated from the initial 3D scan prior to corrosion. The corroded cross-sectional area and radius were evaluated from the XCT data for test types C30 and FC30, while for type C50, A_{cor} was evaluated based on data obtained from 3D scanning of the steel bar after corrosion.

3 Results

In the following, the results from one selected specimen of each type are described. The specimens were selected to be representative of their type, and were less affected by dropouts in the strain measurements along the distributed fibre than the other specimens of similar type.

3.1 Strain measurements

In Fig. 7, strain profiles along the fibre measured after one day of corrosion propagation are presented for one specimen in each series. In these measurements, the strains are relative to the strain in the specimens prior to the corrosion experiment, as a new reference configuration was initialised for each fibre before corrosion started. As can be seen, the strain profiles for

all specimens displayed fluctuating measures of extension and shortening along the fibre length, indicating a non-uniform distribution of radial stress at the surface of the steel. The reason for this behaviour of strain measurements is further discussed in Sect. 3.4. The reference specimen, R30a, had lower peak values of the strain than the specimens with the same geometry subjected to accelerated corrosion, C30a and FC30a. Also, in general, C50c displayed lower peak values than C30a and FC30a.

To study the strain development with time, the mean value of local maxima and minima of each fluctuation cycle were studied (Fig. 7). These mean values and its development with time are shown in Fig. 8 for specimens C30a, FC30a, C50c and R30a. The strain showed the smallest peak values in the reference specimen, R30a. The average strain increment evolved slowly, less than ±50 microstrain, over the entire period in this specimen. For specimen C30a, the average strain increased to approximately ±200 microstrain after five days of corrosion propagation. After seventeen days, the strain decreased slightly but increased again after twenty-six days. Largest strain magnitudes were obtained for specimen C50c (with a larger cover), with 450 and -650 microstrain measured after 12 days and thereafter reducing values. For FC30a (subjected to freeze-thawing before corrosion), the strain increased in magnitude approximately linearly up to ±300 microstrain. Thus, FC30a had slightly larger strain values than the corresponding specimen C30a subjected to corrosion only. Unfortunately, at day twenty-three in the experiment, the fibre broke, which is why no measurements were obtained for FC30a after this period.

3.2 Corrosion level and concrete cracking

XCT was carried out on the specimens of types C30, FC30 and R30 after the corrosion phase. Figure 9 shows one cross-sectional slice for all reference specimens (R30). Cracks in the concrete cover can be identified for all specimens, as indicated with solid arrows. The width of the cover cracks increased with the radial distance from the steel. The XCT data did not reveal corrosion products in the scanned reference specimens, indicating non-corroded condition of the steel. Hence, cover cracking of the reference specimens was probably caused by another mechanism than
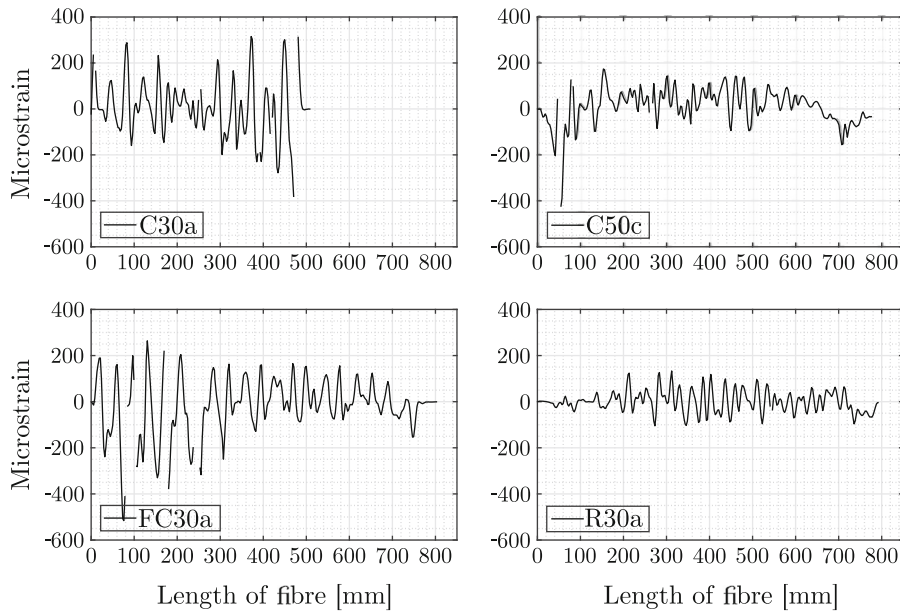
Fig. 7 Profiles of measured strain for four different specimens after one day of impressed current. The strain measurements start from the top surface of the specimens, i.e. the measurements start from the end facing the air and continue downwards in the steel bars. Note that the length of the fibre in specimen C30a is shorter compared to the others, as this particular fibre had fewer turns

Fig. 8 Average strain of local maxima and minima of each fluctuation cycle (Fig. 7), respectively, along the optical fibre, as a function of time. (R)eference, (C)orrosion and (F)rost damaged sample with 30 or 50 mm concrete cover thickness
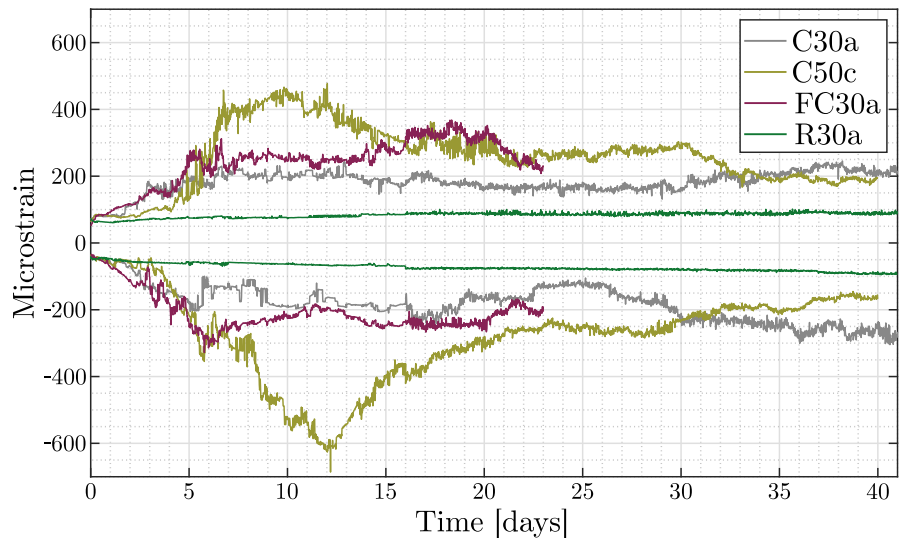
corrosion, most likely concrete shrinkage prior to the start of the corrosion experiment.

In Fig. 10, a contour plot of the corrosion level and XCT data revealing internal concrete cracking close to the steel is shown for C30a, over both the radian and length of the specimen. The left and right vertical boundaries of each figure corresponds to the top and bottom side of the specimen, respectively. The internal cracking in Fig. 10b was evaluated at a radial distance 1.6 mm from the surface of the bar, see circle R1 in Fig. 12a. The evaluation of grey-scale values at the positioning of the circle was done by interpolation of nearest-neighbouring pixels. Note that the corrosion levels are quite large, up to 98%, as they were calculated for the tube, not a solid bar. The corrosion level appears to be non-uniform around the bar, with a
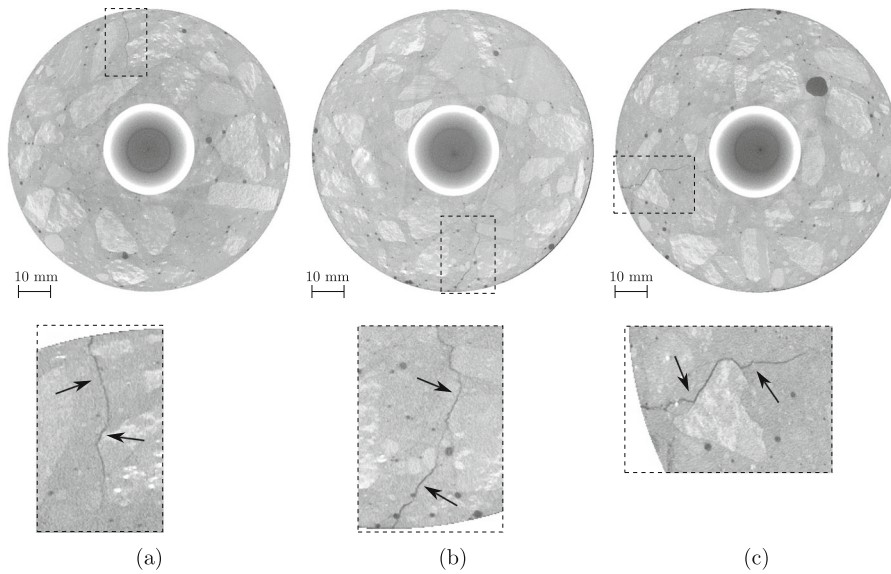
Fig. 9 One cross-sectional slice of **a** R30a, **b** R30b and **c** RC30c, respectively. The images reveal cracking, as indicated by the solid black arrows
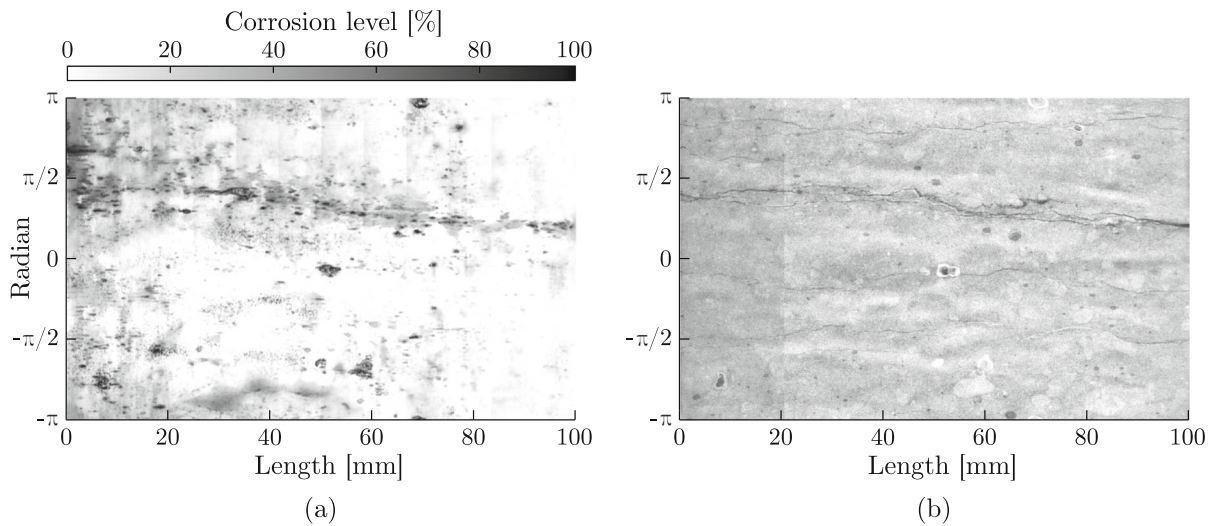
Fig. 10 C30a **a** Corrosion level, and **b** internal cracking as a function of radian and length of the specimen

localised band of corrosion along the length. Interestingly, a larger crack (Fig. 10b) can be seen in the same region. In total, five radial cracks can be identified. Some deep corrosion pits can also be observed (Fig. 10a), and it can be noticed that their location agrees with air voids visible in Fig. 10b.

A validation of the determination of steel mass loss from the image and 3D scanning data is presented in Table 3, which includes additional gravimetric data on the mass loss. In general, a good agreement between the different measures was obtained. The gravimetric mass measurement of R30a confirms the non-corroded state of the steel bar after corrosion, with a small mass loss (considered to be negligible), likely occurring during the sandblasting process. For R30a, the mass loss evaluated from scanning is assumed to correspond to the measurement error of the XCT data.

Table 3 Mass loss of steel evaluated from gravimetric and scanning measures for C30a (3D scanning and XCT), C50c (3D scanning only), FC30a (3D scanning and XCT) and R30a (3D scanning and XCT)

	Gravimetric (%)	Scanning (%)
C30a	7.2	6.4
C50c	5.1	5.6
FC30a	6.1	6.3
R30a	0.3	< 0.6[a]

[a]This measure corresponds to the estimated measurement error from XCT (0.57 %)

3.3 Corrosion level and measured strains

In the following, the interaction between measured strains and corrosion levels is studied. In Fig. 11, strain measurements are superimposed on contour plots of the corrosion level for C50c. The distributed strains correspond to measurements recorded at the end of the corrosion phase. The positioning of the fibre was determined qualitatively by counting the number of turns of the helix and their approximate height per turn. The distribution of the incremental strain can be seen to vary from shortening to extension, as already shown in Fig. 7. In general, in regions where the corrosion level was low, shortening strains can be observed. One localised band with larger corrosion level can be observed along the length of the steel. In
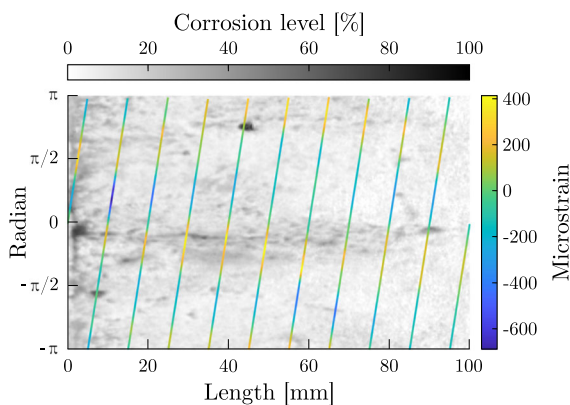
Fig. 11 Specimen C50c: Corrosion level as a function of the radian and length of the specimen. The lines represent the optical fibre and corresponding strain measurements at the last recording

this region, extension strains in the steel were induced. This is further discussed in Sect. 4.

3.4 Corrosion level, cracks and measured strains

The interaction between corrosion level, measured strain in the fibre, and concrete cracking was studied for C30a and FC30a and shown in Fig. 12. Below the cross-sectional slices of the specimens (i.e. Fig. 12a–b), the corresponding distribution of corrosion level and measured strain in the fibre at the end of the corrosion phase are shown (Fig. 12c–d). Analogously, the distribution of concrete cracks are evaluated at three different radial distances from the surface of the steel bars. Figure 12e–f show the distribution of concrete cracks along radial distance R1 for each corresponding specimen, with the measured strain as an overlay. Cracking shown in Figs. 12g–h and 12i–j are evaluated along radial distance R2 and R3, respectively. Close to the SCI, several micro-cracks can be observed (Fig. 12e–f). However, cracking localised into one larger crack for each specimen, as seen in Fig. 12g–j. A localised band of corrosion runs along the length of both specimens, correlating well with the position of the larger cover crack. This indicates that corrosion localised into bands in these regions after cracking of the cover. The hollow steel bars displayed extension strains in the regions where the dominant crack was located. This is clearly visible for FC30b (Fig. 12f), where the peaks in strain along the fibre follows the crack pattern with good precision. For C30a (Fig. 12e), the locations of the peak values in strain correlate well with the crack pattern for the first three turns of the fibre, but deviates slightly for subsequent turns. This deviation is likely due to uncertainties in the positioning of the fibre, which was difficult to determine. For the data presented herein, the extension strains, measured in correspondence to the cover crack, can be interpreted as indicative of stress relief, as the strain measurements are relative to the residual state prior to corrosion.

4 Discussion

The thickness of the concrete cover affected the measured strain in the optical fibre (Fig. 8). For C50c, the strains were larger and the peak occurred later compared to the other specimens. Therefore, a larger
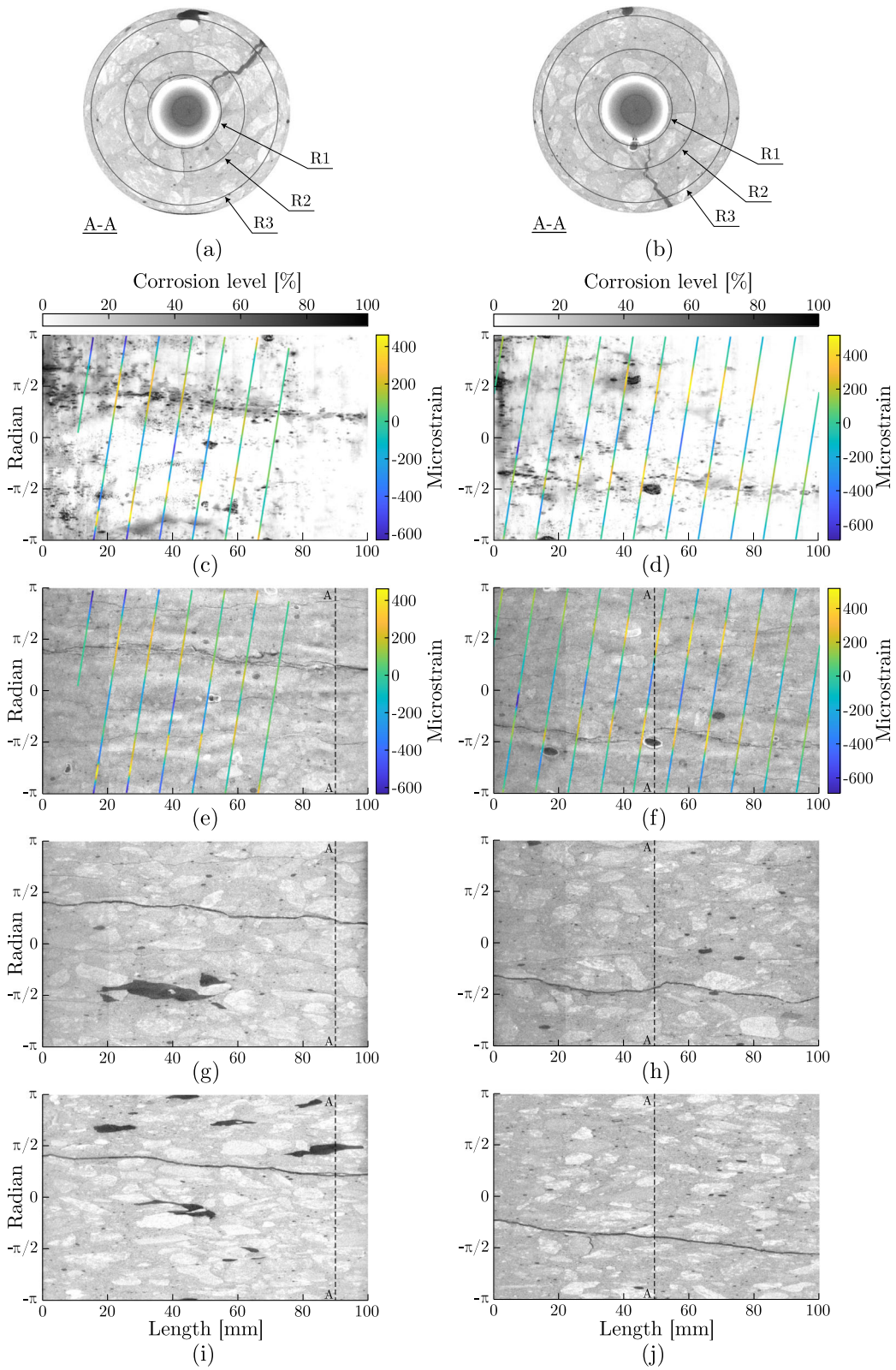
(a)

(b)

(c)

(d)

(e)

(f)

(g)

(h)

(i)

(j)

radial pressure and more energy was required to crack the larger concrete cover. For specimens C30a and FC30a, small differences were observed, as seen in Fig. 8. However, no consistent difference could be observed when comparing measurements on all specimens of type C30 and FC30. This may be related to the small number of freeze and thaw cycles (5) applied prior to corrosion, thus their limited impact on the capacity of the concrete cover [28, 29].

In Fig. 9, the XCT data revealed the presence of longitudinal cracks in the concrete of the reference specimens. These cracks were determined to be unrelated to corrosion, as the steel appeared non-corroded in the XCT data which was further corroborated after sandblasting of the extracted steel, as shown in Table 3. All specimens underwent two drying phases; when the optical fibres were mounted and prior to the XCT scan (see Fig. 1). During these phases, drying shrinkage took place, thus imposing restraint stresses in the specimens prior to the corrosion experiment. Despite cracks were not observed on the surface of the specimens prior to the corrosion experiment, the possibility exists that restraint stresses and subsequently internal micro-cracks were induced by shrinkage. However, as a new reference configuration was established for the fibres with respect to these restraint stresses prior to the corrosion experiment, only the change in strain from this state was monitored (Figs. 7 and 8). Therefore, any quantitative assessment of these restraint stresses in the specimens before corrosion started could not be performed.

The distribution of hoop strain around the steel was found to be non-uniform for all specimens during the complete corrosion experiment, with hoop strains varying from extension to shortening. Additionally, a non-uniform distribution of corrosion products was observed in all specimens exposed to accelerated corrosion, i.e. C50c (Fig. 11), C30a and FC30a (Fig. 12). These specimens showed a localised band

of corrosion along the length of the specimen, which corresponded well with the positioning of the concrete cracks. The strain measurements are an indirect measure of the change in radial stress since the start of the accelerated corrosion (when the optical fibres were re-keyed). Thus, the positive values of the strain measurements may not necessary mean tensile strains; they can instead indicate a reduction of compressive strains. Furthermore, the strain measurements recorded in this study might have been influenced by circumferential shear stresses along the circumference of the steel.

The results in this study are in line with results from previous research. For example, Michel et al. [30] conducted experimental work where deformations around the steel and mortar were monitored, and observed a non-uniform distribution of deformations. These deformations evolved slowly during the first days of corrosion propagation, but increased rapidly as micro-cracks appeared. Furthermore, Ožbolt et al. [14] predicted from a numerical analysis a non-uniform distribution of radial stress at the surface of the steel.

5 Conclusions

This study presents the design of an experimental setup and programme to investigate how corrosion-induced deformations in the steel, concrete cracking and corrosion level interact. The corrosion-induced cracking process was non-destructively monitored using a combination of qualitative and quantitative measures, such as X-ray computed tomography and distributed optical fibre sensors. The experimental programme included four test types, of which three were subjected to accelerated corrosion and one served as a reference. Further, the effect of freeze-thaw damage and concrete cover size were studied. From the work presented in this paper, the following conclusions were drawn:

- The novel test setup presented in this paper shows great potential for detailed studies of the corrosion and cracking processes in reinforced concrete. The test setup involves small-scale laboratory-made samples with hollow steel bars, enabling non-destructive monitoring of strains from the inside of the samples.

- The distribution of strain was found to be non-uniform in the steel during the entire period, with strains varying from extension to contraction along the perimeter of the internal steel surface. This indicates that the distribution of radial stress at the SCI was non-uniform.
- X-ray Computed Tomography was used to acquire image data of the specimens, and by superimposing the strain measurements on contour plots of the image data, it was found that the extension strains were measured in locations of concrete cracking, and contraction strains in between cracks. Further, at the crack locations, corrosion was localised in bands along the steel. These results are in line with previous research [14, 30], but have not been monitored with this level of detail in 3D before.
- The thickness of the concrete cover showed an effect on the corrosion-induced deformations in the steel, where the peak in strain measurement was higher and occurred later for the specimen with larger concrete cover.
- The XCT data revealed longitudinal cracks in the concrete of specimens which were not corroded, most likely caused by drying shrinkage. Thus, drying shrinkage has a significant impact on corrosion-induced cracking, which should be considered in future work.
- There was good agreement between steel mass loss obtained from gravimetric, XCT and 3D scanning data.
- From this study, no significant effects of freeze and thaw cycles on the monitored corrosion-induced deformations were observed. This could possibly relate to the small number of freeze and thaw cycles applied prior to corrosion.

Future work concerns analysis of the stress at the steel-concrete interface including radial and shear stresses, which could be derived from strains measured in the hollow steel bars. Additionally, considering the significant impact of drying shrinkage on corrosion-induced cracking revealed in this study, future research should carefully consider this aspect.

Declarations

References

1. Val DV, Stewart MG, Melchers RE (1998) Effect of reinforcement corrosion on reliability of highway bridges. Eng Struct 20:1010–1019. https://doi.org/10.1016/S0141-0296(97)00197-1
2. Bastidas-Arteaga E, Schoefs F, Stewart MG, Wang X (2013) Influence of global warming on durability of corroding RC structures: a probabilistic approach. Eng Struct 51:259–266. https://doi.org/10.1016/j.engstruct.2013.01.006
3. Stewart MG, Wang X, Nguyen MN (2011) Climate change impact and risks of concrete infrastructure deterioration. Eng Struct 33(4):1326–1337. https://doi.org/10.1016/j.engstruct.2011.01.010
4. Yoon IS, Çopuroğlu O, Park KB (2007) Effect of global climatic change on carbonation progress of concrete. Atmosph Environ 41(34):7274–7285. https://doi.org/10.1016/j.atmosenv.2007.05.028
5. Nasr A, Honfi D, Larsson Ivanov O (2022) Probabilistic analysis of climate change impact on chloride-induced deterioration of reinforced concrete considering Nordic climate. J Infrastr Preserv Resil 3(1):8. https://doi.org/10.1186/s43065-022-00053-6
6. Andrade C, Cesetti A, Mancini G, Tondolo F (2016) Estimating corrosion attack in reinforced concrete by means of crack opening. Struct Concr 17(4):533–540. https://doi.org/10.1002/suco.201500114
7. Tahershamsi M, Fernandez I, Lundgren K, Zandi K (2017) Investigating correlations between crack width, corrosion

level and anchorage capacity. Struct Infrastr Eng 13(10):1294–1307. https://doi.org/10.1080/15732479.2016.1263673

8. Pedrosa F, Andrade C (2017) Corrosion induced cracking: effect of different corrosion rates on crack width evolution. Constr Build Mater 133:525–533. https://doi.org/10.1016/j.conbuildmat.2016.12.030

9. Zhang W, Chen J, Luo X (2019) Effects of impressed current density on corrosion induced cracking of concrete cover. Constr Build Mater 204:213–223. https://doi.org/10.1016/j.conbuildmat.2019.01.230

10. Liu Y, Weyers RE (1998) Modeling the time-to-corrosion cracking in chloride contaminated reinforced concrete structures. ACI Mater J 95(6):675–681

11. Du YG, Chan AHC, Clark LA, Wang XT, Gurkalo F, Bartos S (2013) Finite element analysis of cracking and delamination of concrete beam due to steel corrosion. Eng Struct 56:8–21. https://doi.org/10.1016/j.engstruct.2013.04.005

12. Šavija B, Luković M, Pacheco J, Schlangen E (2013) Cracking of the concrete cover due to reinforcement corrosion: a two-dimensional lattice model study. Constr Build Mater 44:626–638. https://doi.org/10.1016/j.conbuildmat.2013.03.063

13. Fang X, Pan Z, Chen A (2022) Phase field modeling of concrete cracking for non-uniform corrosion of rebar. Theoret Appl Fract Mechan 121:103517. https://doi.org/10.1016/j.tafmec.2022.103517

14. Ožbolt J, Oršanić F, Balabanić G, Kušter M (2012) Modeling damage in concrete caused by corrosion of reinforcement: coupled 3D FE-model. Int J Fract 178:233–244. https://doi.org/10.1007/s10704-012-9774-3

15. Wong HS, Angst UA, Geiker MR, Isgor OB, Elsener B, Michel A et al (2022) Methods for characterising the steel-concrete interface to enhance understanding of reinforcement corrosion: a critical review by RILEM TC 262-SCI. Mater Struct 5(124):1–29. https://doi.org/10.1617/s11527-022-01961-5

16. Angst UM, Geiker MR, Michel A, Gehlen C, Wong H, Isgor OB et al (2017) The steel-concrete interface. Mater Struct Mater Constr 50(2):1–24. https://doi.org/10.1617/s11527-017-1010-1

17. Ahmad S (2003) Reinforcement corrosion in concrete structures, its monitoring and service life prediction-a review. Cement Concr Compos 25:459–471. https://doi.org/10.1016/S0958-9465(02)00086-0

18. Feng W, Tarakbay A, Memon SA, Tang W, Cui H (2021) Methods of accelerating chloride-induced corrosion in steel-reinforced concrete: a comparative review. Construct Build Mater 289:123165. https://doi.org/10.1016/j.conbuildmat.2021.123165

19. Alhede, A (2023) Novel approaches for monitoring effects of steel corrosion in reinforced concrete. Licentiate thesis. https://research.chalmers.se/en/publication/?id=535511

20. Fernandez I, Lundgren K, Zandi K (2018) Evaluation of corrosion level of naturally corroded bars using different cleaning methods, computed tomography and 3D optical scanning. Mater Struct 51(78):13. https://doi.org/10.1617/s11527-018-1206-z

21. EN 197-1 (2011) Cement - Part 1: Composition, specifications and conformity criteria for common cement. Comité Européen de Normalisation (CEN) Europe

22. EN 12390-3 (2019) Testing hardened concrete - Part 3: Compressive strength of test specimens. Comité Européen de Normalisation (CEN) Europe

23. EN 12390-6 (2009) Testing hardened concrete - Part 6: Tensile splitting strength of test specimens. . Comité Européen de Normalisation (CEN) Europe

24. Alonso C, Andrade C, Rodriguez J, Diez JM (1998) Factors controlling cracking of concrete affected by reinforcement corrosion. Mater Struct Mater Constr 31(211):435–441. https://doi.org/10.1007/bf02480466

25. Luna Inc. Optical Distributed Sensor Interrogator. Last accessed 2022-11-21. Available from: https://lunainc.com/product/odisi-6000-series

26. Luna Inc. High-Definition Fiber Optic Strain Sensors. Last accessed 2023-03-06. Available from: https://lunainc.com/product/hd6s

27. Ferreira D. Diana User's Manual: Release 10.5. Available from: https://manuals.dianafea.com/d105/Diana.html

28. Zhang P, Cong Y, Vogel M, Liu Z, Müller HS, Zhu Y et al (2017) Steel reinforcement corrosion in concrete under combined actions: the role of freeze-thaw cycles, chloride ingress, and surface impregnation. Constr Build Mater 148:113–121. https://doi.org/10.1016/j.conbuildmat.2017.05.078

29. Zhang K, Zhou J, Yin Z (2021) Experimental study on mechanical properties and pore structure deterioration of concrete under freeze-thaw cycles. Materials 14(21):6568. https://doi.org/10.3390/ma14216568

30. Michel A, Pease BJ, Peterová A, Geiker MR, Stang H, Thybo AEA (2014) Penetration of corrosion products and corrosion-induced cracking in reinforced cementitious materials: experimental investigations and numerical simulations. Cement Concr Compos 47:75–86. https://doi.org/10.1016/j.cemconcomp.2013.04.011